ELSEVIER

Catalysis Today 74 (2002) 225–234

CATALYSIS TODAY

www.elsevier.com/locate/cattod

X-ray absorption fine structure analysis of local structure of CeO_2–ZrO_2 mixed oxides with the same composition ratio (Ce/Zr = 1)

Yasutaka Nagai [a,*], Takashi Yamamoto [b], Tsunehiro Tanaka [b], Satohiro Yoshida [b], Takamasa Nonaka [a], Tokuhiko Okamoto [a], Akihiko Suda [a], Masahiro Sugiura [a]

[a] *Toyota Central R&D Labs., Inc., Nagakute, Aichi 480-1192, Japan*
[b] *Department of Molecular Engineering, Kyoto University, Kyoto 606-8501, Japan*

Received 28 September 2001; received in revised form 2 November 2001; accepted 30 November 2001

Abstract

Three types of CeO_2–ZrO_2 (Ce:Zr = 1:1 molar ratio) compounds with different oxygen storage/release capacities (OSCs) were characterized by means of the Ce K-edge and Zr K-edge X-ray absorption fine structure (XAFS). In order to investigate the relationship between the OSC and local structure, the quantitative EXAFS curve-fitting analysis was applied. By enhancing the homogeneity of the Ce and Zr atoms in the CeO_2–ZrO_2 solid solution, the OSC performance increased. Especially, the atomically homogeneous $Ce_{0.5}Zr_{0.5}O_2$ solid solution exhibited the highest OSC among these CeO_2–ZrO_2 samples. Additionally, the local oxygen environment around Ce and Zr was remarkably modified by enhancing the homogeneity of the CeO_2–ZrO_2 solid solution. It was postulated that the enhancement of the homogeneity of the CeO_2–ZrO_2 solid solution and the modification of the oxygen environment would be the source for the OSC improvement.

Keywords: Ceria; Zirconia; Oxygen storage capacity; Molecular structure; XAFS

1. Introduction

The oxygen storage/release capacity (OSC) is one of the important functions required for automobile three-way catalysts (TWCs) in order to efficiently remove harmful compounds such as hydrocarbons, CO and NO_x in automotive exhaust gases [1,26]. In the TWCs, ceria is widely used as a promoter due to its high OSC based on the reversible redox reaction ($CeO_2 \leftrightarrow CeO_{2-x} + (x/2)O_2$; $x = 0$–0.5). Ceria stores oxygen under oxygen excess conditions and releases it under oxygen deficient conditions in order to maintain the stoichiometric conditions. The highest catalytic performance is attained at stoichiometric conditions. However, the OSC performance of pure CeO_2 and the durability are still inadequate for practical use, and the improvement of the OSC of CeO_2 is required to develop highly efficient TWCs. Over 10 years ago, our laboratory discovered that the addition of ZrO_2 to CeO_2 would enhance the OSC as well as improve its thermal stability [2–4]. Thereafter, CeO_2–ZrO_2 has been widely utilized for commercial catalysts, and the research on CeO_2–ZrO_2 has been receiving increasing attention. A considerable number of studies have been conducted on the physical properties and structure of CeO_2–ZrO_2 by many groups, and significant progress in knowledge has been made [5–11]. However, the key

* Corresponding author. Fax: +81-561-63-6150.
E-mail address: e1062@mosk.tytlabs.co.jp (Y. Nagai).

0920-5861/02/$ – see front matter
PII: S0920-5861(02)00025-1

factor in improving the OSC by the addition of ZrO_2 to CeO_2 remains unclear. The main purpose of this study is to systematically clarify the relationship between the OSC and the structure of CeO_2–ZrO_2 at the atomic level. Three types of CeO_2–ZrO_2 compounds with the same composition (Ce/Zr = 1) were prepared by different methods, and exhibited different OSC efficiencies. We investigated the local structure around both Ce and Zr of these CeO_2–ZrO_2 samples using the X-ray absorption fine structure (XAFS) method in order to clarify the cation–cation (cation = Ce, Zr) network and the oxygen environment around the cation.

Although several groups have reported the XAFS analyses of CeO_2–ZrO_2, all of them have utilized Ce L_3-edge (5.7 keV) XAFS [6,24] while there have been no studies employing Ce K-edge (40.5 keV) XAFS. The usable data region of Ce L_3-edge EXAFS is limited to ca. 3–9 $Å^{-1}$ in electron wavenumber (k) due to the presence of the Ce L_2-edge (6.2 keV). Since Ce and Zr contributions to the EXAFS signals are remarkable in the high-k part [14], the XAFS measurement of the Ce K-edge with a wide k-range is required to obtain precise information on the Ce–Ce and Ce–Zr bonding, and to clarify the cation–cation network. As a result, conventional characterizations leave controversy about the homogeneity at the atomic level for Ce and Zr atoms in the CeO_2–ZrO_2 solid solution [6,22,23]. The high-energy X-ray at the SPring-8 synchrotron radiation facilities (Hyogo, Japan) makes it possible to record the XAFS spectra with an excellent signal-to-noise ratio at the K-edges of heavy elements, and to obtain precise information on the Ce–cation bonding [12,13,15]. In addition to the foregoing main purpose of clarifying the relationship between the OSC and the atomic structure, another important purpose of this study is to precisely estimate the homogeneity of the CeO_2–ZrO_2 solid solution by both Ce K-edge and Zr K-edge XAFS.

2. Experimental

2.1. Preparation

Three types of CeO_2–ZrO_2 compounds with the same composition (Ce/Zr = 1; CZ55-1, CZ55-2 and CZ55-3) were prepared by the following methods. CZ55-1 was prepared by precipitation with aqueous NH_3 using CeO_2 powder (Anan Kasei, 99.9%, 120 m^2/g) and $ZrO(NO_3)_2$ aqueous solution. The precipitate was dried at 363 K and calcined in air at 773 K for 3 h. CZ55-2 was prepared by coprecipitation with aqueous NH_3 using $Ce(NO_3)_3$ and $ZrO(NO_3)_2$ aqueous solutions. The precipitate was dried at 363 K and calcined in air at 773 K for 3 h. CZ55-3 was synthesized by the same coprecipitation process as CZ55-2, except that the dried powder was reduced at 1473 K for 4 h in flowing pure CO and further oxidized in air at 773 K for 3 h. All the samples were finally calcined in air at 773 K. Oxygen was fully stored in the Ce compounds by this treatment.

2.2. Characterization

2.2.1. OSC measurements

The OSC was estimated by a thermo-gravimetric analysis [11]. The 1 wt.% platinum-loaded CeO_2–ZrO_2 samples were cyclically reduced by 20% H_2 (N_2 balance) for 5 min then oxidized by 50% O_2 (N_2 balance) for 5 min at 773 K. The weight loss and gain were measured using a thermo-gravimetric analyzer (TGA-50, Shimadzu). The reductive/oxidative conditions were maintained until the weight became constant. The value of the weight change between the reductive and oxidative conditions corresponds to the total OSC at 773 K.

2.2.2. Surface area measurements

The specific surface areas of the samples were estimated using the N_2 adsorption isotherm at 77 K by the one-point Brunauer–Emmett–Teller (BET) method using an automatic surface analyzer (Micro Sorp 4232II, Micro Data). The samples were degassed in flowing N_2 at 473 K for 20 min.

2.2.3. X-ray diffraction (XRD)

The powder XRD experiments were carried out using a RINT2000 (Rigaku) diffractometer with Cu Kα radiation (1.5406 Å). The identification of the phase was made with the help of the JCPDS cards (Joint Committee on Powder Diffraction Standards).

2.2.4. XAFS

The Ce K-edge (40.45 keV) and Zr K-edge (18.00 keV) XAFS spectra were measured at BL01B1 and BL16B2 of SPring-8 (Hyogo, Japan). The storage

ring energy was operated at 8 GeV with a typical current of 100 mA. The measurements were carried out using a Si (3 1 1) double crystal monochromator in the transmission mode at room temperature. Data reduction of the XAFS was carried out as described elsewhere [16]. The quantitative curve-fitting analysis of the EXAFS spectra was performed for the inverse Fourier transforms on the cation–cation (cation = Ce, Zr) and cation–oxygen shells. Empirical parameters in the analysis were obtained from standard compounds, e.g. cubic CeO_2 for Ce–Ce and Ce–O bonding, 8 mol% Y-doped cubic ZrO_2 for Zr–Zr and Zr–O bonding, and cubic $Ce_{0.9}Zr_{0.1}O_2$ for Zr–Ce bonding. The parameter for the Ce–Zr bonding was calculated from the extracted Ce–Ce, Zr–Zr and Zr–Ce parameters.

3. Results and discussion

3.1. OSC and BET surface area

Table 1 shows the OSC properties and BET surface area of the samples. The Ce efficiency means the ratio of $Ce^{3+}/(Ce^{3+} + Ce^{4+})$ under reductive conditions. The Zr oxidation state in the CeO_2–ZrO_2 remains at Zr^{4+} under both the reductive and oxidative conditions at 773 K [17]. Thus, only the Ce atoms contribute to the OSC through the Ce^{3+}/Ce^{4+} redox couple. The OSC value increases in the order of CZ55-1 < CZ55-2 < CZ55-3. CZ55-3 exhibited the highest OSC, and its Ce efficiency was 88.6%. It is noteworthy that almost all of the Ce in the CZ55-3 contributes to the OSC. Also, several groups showed that a high temperature reductive treatment followed by a mild oxidation strongly modifies the oxygen release behavior of the CeO_2–ZrO_2 mixed oxide [5,27].

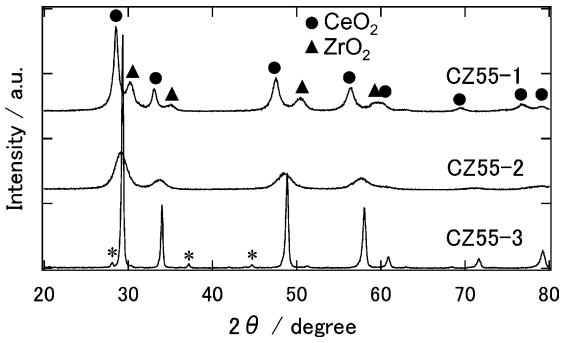

Fig. 1. XRD patterns of CeO_2–ZrO_2 samples with the same composition ratio (Ce/Zr = 1). Small peaks indicated with asterisks are characteristic of κ-$Ce_{0.5}Zr_{0.5}O_2$ due to the ordered arrangement of the cations, see [5].

The BET surface areas ranged from 1 to 125 m^2/g (Table 1). The BET surface areas depend on the preparation methods. Especially, the BET surface area of CZ55-3 is very low due to its high-temperature treatment during its synthesis, indicating that the OSC is not related to the surface area. The number of surface oxygen atoms can be estimated to be ca. 3 μmol-O/m^2 for CeO_2–ZrO_2 (Ce:Zr = 1:1 molar ratio) [18]. The experimental OSC values per meter square of the samples were 1.3, 9.9 and 1500 μmol-O/m^2 for CZ55-1, CZ55-2 and CZ55-3, respectively are OSC (μmol-O/g) divided by BET surface area (m^2/g) in Table 1. Therefore, the oxygen storage/release of CZ55-1 is limited to the surface at 773 K. In the case of CZ55-2, the oxygen storage/release progresses from the surface to ca. three layers. For CZ55-3, almost all the bulk oxygen atoms contribute to the OSC.

3.2. XRD

Fig. 1 shows the XRD patterns of the samples. The phase identification of the samples is summarized in

Table 1
OSC property and BET surface area of CeO_2–ZrO_2 mixed oxides

Sample[a]	OSC (μmol-O/g)[b]	Ce efficiency (%)[c]	BET surface area (m^2/g)
CZ55-1	160	9.6	125
CZ55-2	880	51.7	89
CZ55-3	1500	88.6	1

[a] For sample description, see Section 2.
[b] OSC (oxygen storage/release capacity) of 1 wt.% Pt-loaded Ce compounds was measured at 773 K.
[c] The ratio of $Ce^{3+}/(Ce^{3+} + Ce^{4+})$ under reductive condition.

Table 2
Phases identified and lattice parameters determined by XRD

Sample	Phase	Lattice parameters (Å)
CeO_2[a]	Cubic	$a = 5.41$
CZ55-1	Cubic (CeO_2)	$a = 5.41$
	Tetragonal (ZrO_2)	$a = 3.58$, $c = 5.21$
CZ55-2	Cubic	$a = 5.29$
CZ55-3	Cubic	$a = 5.26$

[a] Standard compound. The data refer to JCPDS cards number 34-0394.

Table 2. Broad XRD peaks were observed for CZ55-1 and CZ55-2, while sharp peaks for CZ55-3. CZ55-1 was shown to be a mixture of cubic CeO_2 (lattice parameter: $a = 5.41$ Å) and tetragonal ZrO_2 (lattice parameter: $a = 3.58$ Å, $c = 5.21$ Å), although CZ55-2 and CZ55-3 have a cubic structure (lattice parameter: CZ55-2, $a = 5.29$ Å; and CZ55-3, $a = 5.26$ Å). The lattice constants of the cubic phase for the samples decrease in the order of CZ55-1, CZ55-2 and CZ55-3. This means that the unit cell of the cubic phase shrinks in this order.

In CZ55-3, we could observe small peaks indicated with an asterisk, except for the principal peaks which are attributed to the cubic CeO_2–ZrO_2. These small peaks are due to the ordered arrangement of the cations [9]. It is well known that a pyrochlore-type $Ce_2Zr_2O_7$ forms by the high temperature reduction of CeO_2–ZrO_2, which possesses the ordered arrangement of Ce and Zr ions [5]. The κ-$Ce_{0.5}Zr_{0.5}O_2$ phase is prepared by mild-oxidation of the pyrochlore-type precursor, which maintains the ordered arrangement [5]. The XRD patterns of CZ55-3 almost correspond to that of κ-$Ce_{0.5}Zr_{0.5}O_2$. Therefore, it is suggested that CZ55-3 is cubic CeO_2–ZrO_2 with an ordered arrangement of the cations.

3.3. XAFS

3.3.1. Fourier transforms (FTs) of Ce K-edge and Zr K-edge EXAFS spectra

FTs were performed on the Ce and Zr K-edges EXAFS spectra in about the 3.0–17 $Å^{-1}$ region. The FTs of the Ce K-edge EXAFS spectra are presented in Fig. 2(a). The first peak at 1.8 Å and the second peak at 3.5 Å correspond to the Ce–O and Ce–cation (cation = Ce, Zr) bonds, respectively. The position and amplitude of the Ce–O peaks for CZ55-1, CZ55-2 and CZ55-3 are slightly different from each other. CZ55-2 and CZ55-3 exhibit lower Ce–cation peak intensities than that of CZ55-1. Additionally, the Ce–cation peak of CZ55-3 appears to have split in two. These clear differences among the Ce–cation peaks could not be observed for the Ce L_3-edge (Fig. 2(b)). Especially, the Ce–cation peaks of CZ55-2 and CZ55-3 in the Ce L_3-edge almost disappear due to the lack of an EXAFS signal for heavy elements in the high-*k* part. Therefore, the measurements of the Ce K-edge XAFS spectrum are necessary to obtain precise information about the Ce–cation bonding. Fig. 3 shows the FTs of the Zr K-edge EXAFS spectra. The first peak at 1.7 Å was assigned to Zr–O bonds and the second peak at

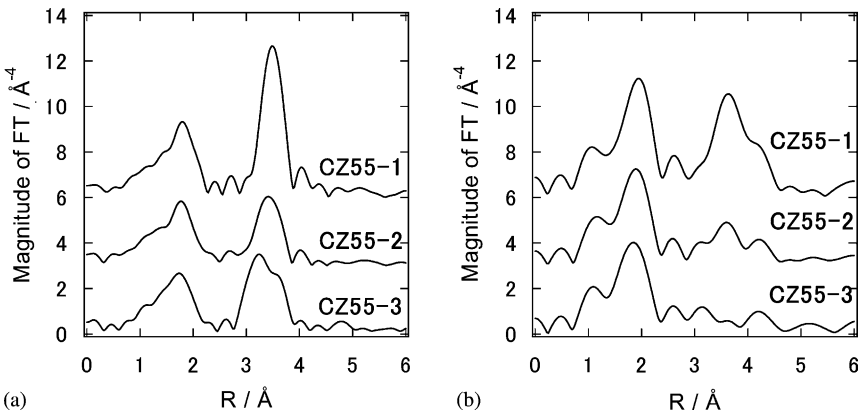

Fig. 2. Fourier-transformed $k^3\chi$ data of (a) Ce K-edge and (b) Ce L_3-edge EXAFS of CeO_2–ZrO_2 samples.

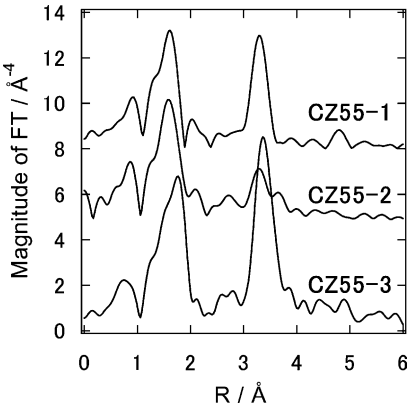

Fig. 3. Fourier-transformed $k^3\chi$ data of Zr K-edge EXAFS of CeO_2–ZrO_2 samples.

3.5 Å to Zr–cation bonds. The shape of the FTs for CZ55-1, CZ55-2 and CZ55-3 are obviously different. According to the results mentioned above, it is thus suggested that the OSC exhibits a significant correlation with the local structure around Ce and Zr.

3.3.2. Zr K-edge XANES spectra

The XANES spectra at the Zr K-edge are shown in Fig. 4. A comparison of the spectra indicated by A or B was carefully made. To begin with, peak A, a weak shoulder on the steeply rising absorption edge, is more apparent in CZ55-1 and CZ55-2 than in CZ55-3. This pre-edge absorption can be assigned to the 1s → 4d which is sensitive to the cation–O geometry. This transition is stronger in compounds that are distorted from centrosymmetry, and significantly appear for pure tetragonal ZrO_2 [19]. In fact, the feature of the XANES spectrum of CZ55-1 is very similar to that of pure tetragonal ZrO_2 [19]. Furthermore, tetragonal ZrO_2 was identified by the XRD result described above. CZ55-2 also possesses a tetragonal environment of the Zr–O coordination. On the other hand, it is postulated that CZ55-3 possesses a higher centrosymmetry of Zr–O coordination than those of CZ55-1 and CZ55-2. The feature of the XANES spectrum of CZ55-3 is very similar to that of cubic ZrO_2 [19]. Next, peak B in CZ55-1 shows a single broad peak, whereas that in CZ55-2 shows a slight splitting, and in CZ55-3, a clear splitting. A similar splitting has been reported for the Y_2O_3–ZrO_2 solid solution by Li et al. [20]. Li et al. reported that the splitting becomes progressively more pronounced as the Y_2O_3 concentration increases from 3 mol% Y_2O_3–ZrO_2 (tetragonal) to 20 mol% Y_2O_3–ZrO_2 (cubic). They also observed that peak A decreases with the increasing Y_2O_3 concentration. Therefore, the results derived from the XANES spectra in our

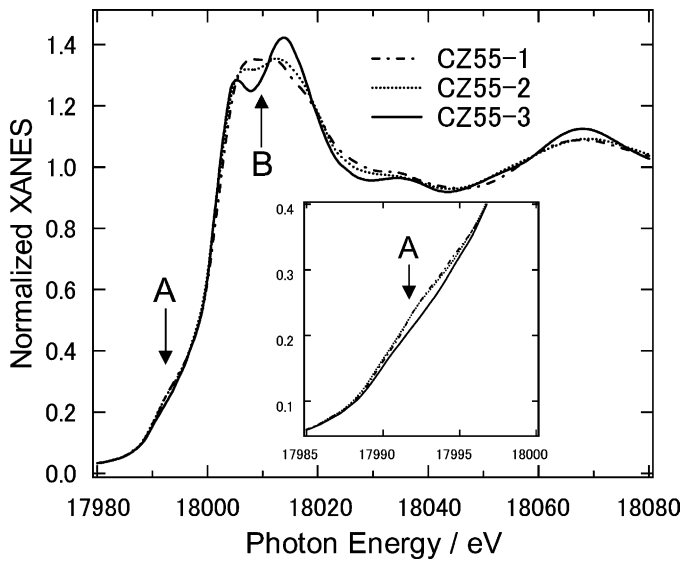

Fig. 4. Zr K-edge XANES spectra of CeO_2–ZrO_2 samples.

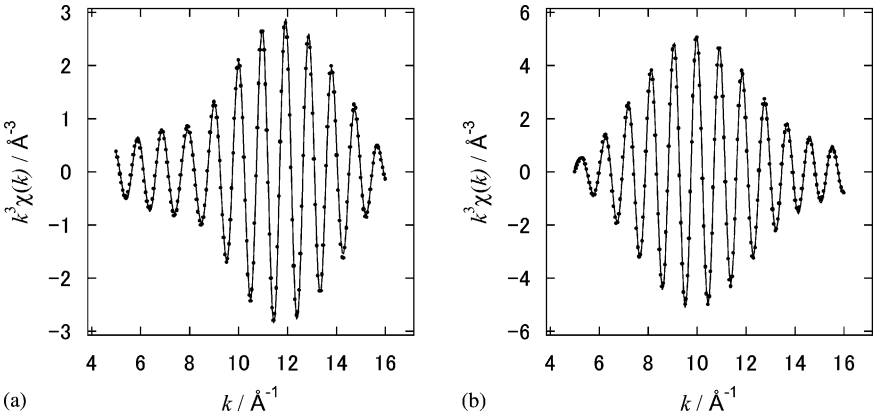

Fig. 5. Inverse Fourier transforms of (a) Ce–cation and (b) Zr–cation shells for CZ55-3 and the corresponding curve-fit. Experimental (—) and curve-fit (●).

system indicate that the concentration of Ce insertion into ZrO_2 increases along the series: CZ55-1, CZ55-2 and CZ55-3. Additionally, as more CeO_2 is inserted into the ZrO_2 lattice, the CeO_2–ZrO_2 is expected to form a more cubic structure.

3.3.3. Cation–cation network

A quantitative curve-fitting analysis was performed for the cation–cation shells in the FTs to clarify this network. For example, Fig. 5 shows the fit of inverse FTs of the cation–cation shells for CZ55-3. The curve-fitting results of the Ce and Zr K-edges EXAFS are summarized in Tables 3 and 4, respectively. Fig. 6 shows a model illustration of the cation–cation network for the CeO_2–ZrO_2 samples, which is proposed from the curve-fitting analysis. First, the Ce–cation shell for CZ55-1 was fitted with a single Ce–Ce bond, and the Zr–cation shell was also fitted with a single Zr–Zr bond. The distance ($R = 3.82$ Å) and coordination number (CN = 11.9) of the Ce–Ce bond is consistent with the values for CeO_2. Thus CZ55-1 is a mixture of pure CeO_2 and ZrO_2 (Fig. 6(a)). The CN of the Zr–Zr bond for CZ55-1 (6.6) is lower than 12. It could be considered that the size of the formed ZrO_2 crystallite was small. The average particle size was estimated from the XRD peak using the Scherrer equation. The particle sizes of CeO_2 and ZrO_2 in CZ55-1 were about 130 and 80 Å, respectively. This result supports the decrease in the CN of the Zr–Zr bond for CZ55-1. Secondly, for CZ55-2, not only Ce–Ce (Zr–Zr), but also Ce–Zr (Zr–Ce) bonds were required to obtain an appropriate fit for the cation–cation shell at the Ce (Zr) K-edge. The Ce–cation shell was fitted with Ce–Ce (CN = 8.0)

Table 3
Results of curve-fitting analysis for Ce–cation shells[a]

Sample	Bond	CN	R (Å)	$\Delta\sigma^2$ (Å^2)[b]
Cubic CeO_2[c]	Ce–Ce	12	3.826	
CZ55-1	Ce–Ce	11.9(2)	3.82(0)	0.0026(1)
CZ55-2	Ce–Ce	8.0(4)	3.78(0)	0.0034(2)
	Ce–Zr	3.6(5)	3.71(0)	0.0063(13)
CZ55-3	Ce–Ce	6.0(3)	3.78(0)	0.0016(2)
	Ce-Zr	6.0(3)	3.72(0)	0.0022(3)

[a] The standard deviation is given in the parentheses.
[b] Relative Debye–Waller factor.
[c] Standard compound.

Table 4
Results of curve-fitting analysis for Zr–cation shells[a]

Sample	Bond	CN	R (Å)	$\Delta\sigma^2$ (Å^2)[b]
Cubic ZrO_2[c]	Zr–Zr	12	3.628	
CZ55-1	Zr–Zr	6.6(2)	3.66(0)	0.0061(1)
CZ55-2	Zr–Zr	3.0(6)	3.69(0)	0.0124(19)
	Zr–Ce	4.0(3)	3.76(0)	0.0030(3)
CZ55-3	Zr–Zr	6.0(4)	3.62(0)	0.0086(6)
	Zr–Ce	6.0(3)	3.75(0)	−0.0010(1)

[a] The standard deviation is given in the parentheses.
[b] Relative Debye–Waller factor.
[c] 8 mol% Y-doped cubic ZrO_2 as standard compound.

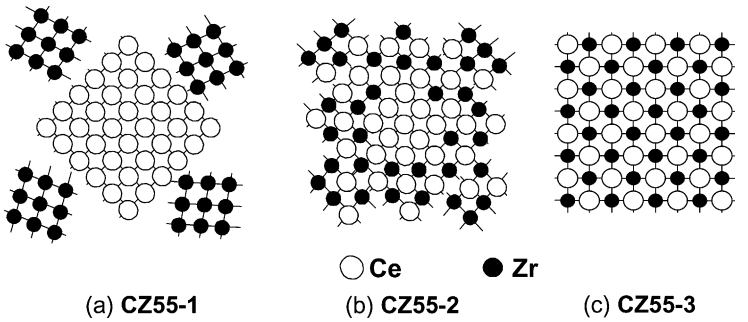

Fig. 6. Model illustration of cation–cation network for the CeO_2–ZrO_2 samples with the same composition (Ce/Zr = 1). CZ55-1 consists of pure CeO_2 and ZrO_2. A CeO_2–ZrO_2 solid solution forms in CZ55-2, but the Ce rich domain and Zr rich one still remain. The $Ce_{0.5}Zr_{0.5}O_2$ solid solution in CZ55-3 homogeneously forms at an atomic level, and possesses the ordered arrangement of Ce and Zr ions.

and Ce–Zr (CN = 3.6) bonds. The CN of the Ce–Ce bond is larger than that of the Ce–Zr bond. The CN of the Ce–Zr bond (3.6) is close to that of the Zr–Ce bond (4.0). This indicates that a CeO_2–ZrO_2 solid solution in CZ55-2 forms, but a Ce rich domain and Zr rich one still remain (Fig. 6(b)). As for the Zr–Zr bond of CZ55-2, we could not obtain the appropriate fit. The relative Debye–Waller factor ($\Delta\sigma^2$) is too large. This may mean that the distribution of the Zr–Zr bond distances is broad due to the presence of some structural disorder. Finally, the Ce–cation shell for CZ55-3 was fitted with Ce–Ce (CN = 6.0) and Ce–Zr (CN = 6.0) bonds. The Zr–cation shell was also fitted with Zr–Zr (CN = 6.0) and Zr–Ce (CN = 6.0) bonds. The CN ratios of Ce–Ce to Ce–Zr and Zr–Zr to Zr–Ce are just 1. These CN ratios are equal to the Ce/Zr composition ratio of the sample. It is clear that the $Ce_{0.5}Zr_{0.5}O_2$ solid solution in CZ55-3 homogeneously forms at an atomic level. Furthermore, as we mentioned in the XRD section, CZ55-3 possesses an ordered arrangement of Ce and Zr ions (Fig. 6(c)). The homogeneity of the CeO_2–ZrO_2 solid solution increases in the order of CZ55-1, CZ55-2 and CZ55-3. This is in agreement with the suggestion derived from the result of the Zr K-edge XANES. These results lead to the conclusion that the OSC increases by enhancing the homogeneity of the Ce and Zr atoms in the CeO_2–ZrO_2 solid solution.

3.3.4. Oxygen environment around cation

We will now discuss the cation–oxygen shells of these samples. Tables 5 and 6 present the curve-fitting results for the Ce–oxygen and Zr–oxygen shells, respectively. First, the CN of Ce–O for all samples was eight. The Ce–O bond length (R = 2.33 Å) of CZ55-1 is almost consistent with that of CeO_2 as a standard compound. In contrast, the Ce–O bond length gradually shortens in the order of CZ55-1, CZ55-2 and CZ55-3. Since the CeO_2–ZrO_2 solid solution in CZ55-2 is nonhomogeneous, its Ce–O bond length is the average value of all the Ce–O bonds.

Table 5
Results of curve-fitting analysis for Ce–oxygen shells[a]

Sample	Bond	CN	R (Å)	$\Delta\sigma^2$ (Å^2)[b]
Cubic CeO_2[c]	Ce–O	8	2.343	
CZ55-1	Ce–O	8.0(1)	2.33(0)	0.0035(1)
CZ55-2	Ce–O	8.0(1)	2.30(0)	0.0052(3)
CZ55-3	Ce–O	8.0(2)	2.27(0)	0.0044(2)

[a] The standard deviation is given in the parentheses.
[b] Relative Debye–Waller factor.
[c] Standard compound.

Table 6
Results of curve-fitting analysis for Zr–oxygen shells[a]

Sample	Bond	CN	R (Å)	$\Delta\sigma^2$ (Å^2)[b]
Cubic ZrO_2[c]	Zr–O	8	2.222	
CZ55-1	Zr–O	4.0(5)	2.17(0)	−0.0081(5)
	Zr–O	4.0(6)	2.36(0)	0.0067(28)
CZ55-2	Zr–O	6.0(5)	2.19(0)	−0.0059(4)
	Zr–O	2.0(5)	2.37(3)	−0.0017(11)
CZ55-3	Zr–O	8.0(2)	2.27(0)	−0.0046(2)

[a] The standard deviation is given in the parentheses.
[b] Relative Debye–Waller factor.
[c] 8 mol% Y-doped cubic ZrO_2 as standard compound.

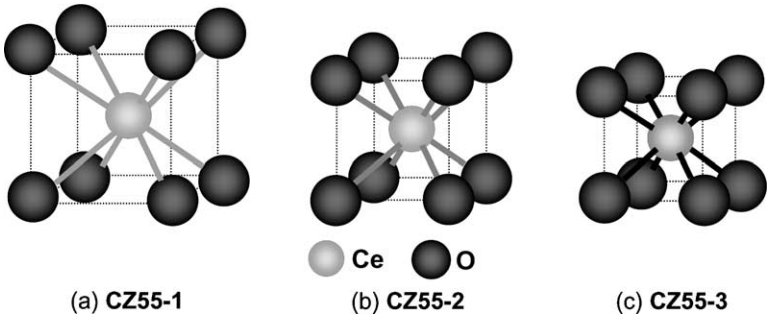

Fig. 7. Model illustration of oxygen environment around Ce. The Ce–O bond length gradually shortens in the order of CZ55-1, CZ55-2 and CZ55-3.

A model illustration of the oxygen environment around Ce is proposed in Fig. 7. This phenomenon of the gradual compression of the Ce–O bonding is interpreted as follows. Since the ionic radius of Zr^{4+} (0.84 Å) for an 8-fold coordination is smaller than that of Ce^{4+} (0.97 Å) [21], the unit cell of the cubic CeO_2–ZrO_2 solid solution decreases with the increasing undersized Zr^{4+} concentration inserted into the Ce network, causing the Ce–O bond length to shorten. The decreasing of the lattice constant for the CeO_2–ZrO_2 samples result supports this result for the compression of the Ce–O bonding.

Secondly, the Zr–O bond for CZ55-1 was fitted with two sets of short and long Zr–O bond lengths. Its bond length and the CN of Zr–O are close to the values for typical tetragonal ZrO_2 [19]. The Zr–O bond for CZ55-2 also consisted of two sets of Zr–O bond lengths. However, the CN of the Zr–O bond for CZ55-2 (6 + 2) is different from that (4 + 4) for a typical tetragonal ZrO_2. In contrast, the Zr–O bond for CZ55-3 was fitted with a single Zr–O bond. The model illustration of the oxygen environment around Zr is proposed in Fig. 8. This phenomenon is interpreted as follows. In CZ55-1, a pure tetragonal ZrO_2 forms and has two sets (4 + 4) of short and long Zr–O bond lengths. For CZ55-2, the symmetry of the Zr–O coordination is, on average, somewhat more centrosymmetric than that of the tetragonal ZrO_2 due to the introduction of some Zr ions into the cubic CeO_2 framework. Because of the nonhomogeneous CeO_2–ZrO_2 solid solution in CZ55-2, Fig. 8(b) indicates the average structure of the oxygen environment around all the Zr atoms, and its average structure is an intermediate state between CZ55-1 and CZ55-3. For CZ55-3,

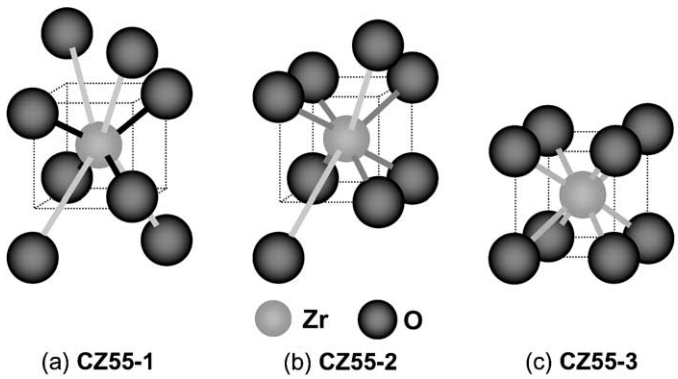

Fig. 8. Model illustration of oxygen environment around Zr. In CZ55-1, a pure tetragonal ZrO_2 forms and has two sets of short and long Zr–O bond lengths. For CZ55-2, the symmetry of Zr–O coordination is, on average, somewhat more centrosymmetric than that of tetragonal ZrO_2. The configuration of the oxygen around Zr for CZ55-3 has a good symmetric 8-fold coordination.

a cubic $Ce_{0.5}Zr_{0.5}O_2$ solid solution homogeneously forms at the atomic level. Hence, the configuration of the oxygen around Zr for CZ55-3 has a good symmetric 8-fold coordination. These results are in accord with the Zr K-edge XANES observations that CZ55-3 possesses a higher centrosymmetry of Zr–O coordination than those of CZ55-1 and CZ55-2.

3.4. Mechanism of the OSC improvement

Here, we discuss the mechanism of the OSC improvement from the points of the homogeneity and the oxygen environment. First, the effective ionic radii of Ce^{4+}, Ce^{3+} and Zr^{4+} are 0.97, 1.14 and 0.84 Å, respectively [21]. During the oxygen release process, the volume of the Ce compound increases in proportion to the change of the Ce oxidation state from Ce^{4+} to Ce^{3+}. The stress energy arising from this volume increment would restrict any further valence change of the Ce. The introduction of downsized Zr ions into the Ce framework could compensate for the volume increment, and ease the valence change ($Ce^{4+} \rightarrow Ce^{3+}$). In fact, a computer simulation study by Balducci et al. [25] indicates that the Ce^{4+}/Ce^{3+} bulk reduction energy in model cubic CeO_2–ZrO_2 solid solutions was significantly reduced even with small amounts of ZrO_2. This point would be the main reason why the enhancement of the homogeneity of Ce and Zr atoms in the CeO_2–ZrO_2 solid solution improves the OSC performance. Secondly, by the atomically homogeneous introduction of Zr ions into the cubic CeO_2 framework, the Ce–O bond length shortens, and the configuration of the oxygen around Zr has a more centrosymmetric coordination. In particular, CZ55-3 has a good symmetric 8-fold coordination around the Zr. This symmetric 8-fold coordination state around Zr is generally considered to be spatially tight and unstable, because the ionic radius of Zr^{4+} (0.84 Å) is much smaller than that of O^{2-} (1.38 Å) [21]. On the other hand, the oxygen environment around Ce for CZ55-3 is also considered to be tight, because the Ce–O bond length for CZ55-3 is much shorter than that for the stable pure CeO_2. Actually, CZ55-3, the κ-$Ce_{0.5}Zr_{0.5}O_2$ solid solution, is not a stable phase but a metastable one in an oxidative atmosphere [5]. At 1273 K or less, CZ55-3 maintains its structure. However, if the temperature goes over 1473 K, a phase separation occurs in the oxidative atmosphere, and part of the CZ55-3 is divided into stable CeO_2 and ZrO_2. We confirmed these phenomena by XRD. This instability of the oxygen environment around Ce and Zr will generate some active oxygens which are responsible for the improved OSC. However, our suggestion about the Zr–O local structure for the improved OSC differs from previous results. For example, Vlaic et al. [6] reported the following: "by introducing Zr ions into the CeO_2 lattice, the oxygen sublattice becomes significantly distorted. Zr–O coordination of the type 4 + 2 (short and long Zr–O) is found due to a displacement of two oxygens to a nonbonding distance. This distortion of the oxygen sublattice generates some mobile oxygens." On the other hand, Lemaux et al. [10] reported the following: "a lamellar-type structural model explains the high OSC of $Ce_{0.5}Zr_{0.5}O_2$, the short Zr–O_I (CN = 4) corresponds to the *intralayer* Zr–O bond and the much weaker and long Zr–O_{II} (CN = 4) to the interlayer Zr–O interaction. The OSC is determined by the interlayer Zr–O interaction." In both cases, they insist that the distortion of the short and long Zr–O coordination enhances the OSC. In contrast, we suggest that the instability of the symmetric 8-fold coordination around Zr, as shown in CZ55-3, will generate some active oxygens. Vlaic and Lemaux et al. investigated the local structure of the CeO_2–ZrO_2 solid solution prepared by a high temperature firing or a precipitation process, not by a high temperature reduction. A high temperature reductive treatment followed by a mild oxidation causes the ordered arrangement of the cations, and that treatment could construct a specific oxygen environment around the cations. However, at present, we have no definite explanation for these different opinions. Further work is required to estimate the general validity.

4. Concluding remarks

The present study clearly showed the relationship between the OSC and local structure around Ce and Zr in three types of CeO_2–ZrO_2 mixed oxides (Ce:Zr = 1:1 molar ratio). In conclusion, the OSC increases by enhancing the homogeneity of the Ce and Zr atoms in the CeO_2–ZrO_2 solid solution. Especially, an atomically homogeneous $Ce_{0.5}Zr_{0.5}O_2$ solid solution exhibited the highest OSC among these CeO_2–ZrO_2 samples. The enhancement of the

homogeneity of the Ce and Zr atoms could ease the valence change of the Ce ($Ce^{4+} \rightarrow Ce^{3+}$). By the atomically homogeneous introduction of Zr ions into the cubic CeO_2 framework, the Ce–O bond length in the CeO_2–ZrO_2 shortens, and the configuration of the oxygen around Zr has a more centrosymmetric 8-fold coordination. This modification of the local oxygen environment around Ce and Zr will generate some active oxygens for the OSC improvement. We postulated that the enhancement of the homogeneity of the CeO_2–ZrO_2 solid solution and the modification of the oxygen environment would be the source for the OSC improvement. Additionally, we could clarify the cation–cation network by using the high-energy X-ray at SPring-8, and precisely estimate the homogeneity at the atomic level of the CeO_2–ZrO_2 solid solution.

The mechanism of the OSC improvement is not yet completely understood. Especially, the oxygen environment around cations remains a matter of debate. The XAFS analysis only provides the average local structure. To clarify this point, we have to obtain detailed information on the structure of the homogeneous CeO_2–ZrO_2 solid solution. We plan to investigate the precise crystal structure of the homogeneous CeO_2–ZrO_2 solid solution by using synchrotron X-ray and pulsed neutron scattering.

Finally, through this research, we have determined an important guide that catalyst design at the atomic level is necessary in order to develop high performance catalysts for practical use.

Acknowledgements

The X-ray absorption experiments were performed at the SPring-8 with the approval of the Japan Synchrotron Radiation Research Institute (JASRI) (Proposal No. 2000A0143-NX-np and C99B16B2-417N).

References

[1] S. Matsumoto, Toyota Tec. Rev. 44 (1994) 10.
[2] Japanese Unexamined Patent Publication, 116741 (1988).
[3] S. Matsumoto, N. Miyoshi, T. Kanazawa, M. Kimura, M. Ozawa, in: S. Yoshida, N. Tabezawa, T. Ono (Eds.), Catalysis Science and Technology, Vol. 1, Kodansha/VCH, Tokyo/Weinheim, 1991, p. 335.
[4] M. Ozawa, M. Kimura, A. Isogai, J. Alloys Comp. 193 (1993) 73.
[5] T. Omata, H. Kishimoto, S. Otsuka-Yao-Matsuo, N. Ohtori, N. Umesaki, J. Solid State Chem. 147 (1999) 573.
[6] G. Vlaic, P. Fornasiero, S. Geremia, J. Kašpar, M. Granziani, J. Catal. 168 (1997) 386.
[7] Y. Madier, C. Descorme, A.M. Le Govic, D. Duprez, J. Phys. Chem. B 103 (1999) 10999.
[8] E. Mamotov, T. Egami, R. Brezny, M. Koranne, S. Tyagi, J. Phys. Chem. B 101 (2000) 11110.
[9] H. Kishimoto, T. Omata, S. Otsuka-Yao-Matsuo, K. Ueda, H. Hosono, H. Kawazoe, J. Alloys Comp. 312 (2000) 94.
[10] S. Lemaux, A. Bensaddik, A.M.J. van der Earden, J.H. Bitter, D.C. Koningsberger, J. Phys. Chem. B 105 (2001) 4810.
[11] A. Suda, H. Sobukawa, T. Suzuki, T. Kandori, Y. Ukyo, M. Sugiura, J. Ceram. Soc. Jpn. 109 (2001) 177.
[12] Y. Nagai, T. Yamamoto, T. Tanaka, S. Yoshida, T. Nonaka, T. Okamoto, A. Suda, M. Sugiura, J. Synchrotron Rad. 8 (2001) 616.
[13] Y. Nagai, T. Yamamoto, T. Tanaka, SPring-8 Research Frontiers, 1999/2000, p. 46.
[14] B.K. Teo, EXAFS: Basic Principles and Data Analysis, Springer, Berlin, 1986.
[15] T. Uruga, H. Tanida, Y. Yoneda, K. Takeshita, S. Emura, M. Takahashi, M. Harada, Y. Nishihata, Y. Kubozono, T. Tanaka, T. Yamamoto, H. Maeda, O. Kamishima, Y. Takabayashi, Y. Nakata, H. Kimura, S. Goto, T. Ishikawa, J. Synchrotron Rad. 6 (1999) 143.
[16] T. Tanaka, H. Yamashita, R. Tsutitani, T. Funabiki, S. Yoshida, J. Chem. Soc., Faraday Trans. 84 (1988) 2987.
[17] P. Fornasiero, R. Di Monte, G. Rao Ranga, J. Kašpar, S. Meriani, A. Trovarelli, M. Granziani, J. Catal. 151 (1995) 168.
[18] T. Tanabe, A. Suda, C. Deccorme, D. Duprez, H. Shinjoh, M. Sugiura, Stud. Surf. Sci. Catal. 138 (2001) 135.
[19] P. Li, I.-W. Chen, J.E. Penner-Hahn, Phys. Rev. B 48 (1993) 10063.
[20] P. Li, I.-W. Chen, J.E. Penner-Hahn, Phys. Rev. B 48 (1993) 10074.
[21] R.D. Shannon, C.T. Prewitt, Acta Cryst. B25 (1969) 925.
[22] Y.K. Voronko, A.A. Sobol, V.A. Ushakov, L.Y. Tsymbal, Inorg. Mater. 30 (1994) 747.
[23] T. Hirata, E. Asari, M. Kitajima, J. Solid State Chem. 110 (1994) 201.
[24] P. Li, I.-W. Chen, J.E. Penner-Hahn, J. Am. Ceram. Soc. 77 (1994) 1281.
[25] G. Balducci, J. Kašpar, P. Fornasiero, M. Granziani, M.S. Islam, J.D. Gale, J. Phys. Chem. B 101 (1997) 1750.
[26] H.C. Yao, Y.F. Yao, J. Catal. 86 (1984) 254.
[27] P. Fornasiero, G. Balducci, R. Di Monte, J. Kašpar, V. Sergo, G. Gubitosa, A. Ferrero, M. Granziani, J. Catal. 164 (1996) 173.